Renewable Energy 175 (2021) 926–935

Contents lists available at ScienceDirect

Renewable Energy

journal homepage: www.elsevier.com/locate/renene

Effects of atmospheric stability on the performance of a wind turbine located behind a three-dimensional hill

Luoqin Liu *, Richard J.A.M. Stevens **

Physics of Fluids Group, Max Planck Center Twente for Complex Fluid Dynamics, J. M. Burgers Center for Fluid Dynamics and MESA+ Research Institute, University of Twente, P.O. Box 217, 7500, AE, Enschede, the Netherlands

ARTICLE INFO

Article history:
Received 9 January 2021
Received in revised form
19 April 2021
Accepted 5 May 2021
Available online 10 May 2021

Keywords:
Atmospheric boundary layer
Atmospheric stability
Large eddy simulation
Power output
Three-dimensional hill
Wind turbine wake

ABSTRACT

Understanding the effect of thermal stratification on wind turbine wakes in complex terrain is essential to optimize wind farm design. The effect of a three-dimensional hill on the performance of a downwind turbine is studied by performing large eddy simulations for different atmospheric conditions. The distance between the hill and the turbine is six times the turbine diameter, and the hill height is equal to the hub height. It is shown that the hill wake reduces the power production of the downstream turbine by 35% for the convective boundary layer case under consideration. However, surprisingly, the wind turbine power production is increased by about 24% for the stable boundary layer case considered here. This phenomenon results from the entrainment of kinetic energy from the low-level jet due to the increased mixing induced by the hill wake. This effect strongly depends on the Coriolis force-induced wind veer. The increased turbulence intensity by the hill results in a strong increase in the forces experienced by the blades, which suggest the turbine is experiencing much higher unsteady turbulence loading. It is shown that the increase in the power fluctuations may not fully reflect the increase in the force fluctuations on the blades.

1. Introduction

As more and more wind turbines will be installed in complex terrains, it is crucial to study the effect of atmospheric stability on the performance of wind turbines in hilly terrain [1–3]. This will help wind energy assessment and models that are used to optimize wind turbine siting. A significant amount of research has been carried out to investigate the effect of topography on wind turbine performance. Most of these studies were performed under neutral stratification conditions [4–12]. However, only a few studies considered the effect of thermal stratification in complex terrain [13–18].

To the best knowledge of the authors, the experimental investigation of hills effect on the performance of wind turbines began in the early 1990s [4,19]. For an isolated two-dimensional hill, Tian et al. [6] found experimentally that the wind speed was much higher, and the turbulence intensity was relatively low, on the top and the windward side of the hill. Therefore, they recommended placing turbines in these locations. This finding was later confirmed by the large eddy simulations (LES) performed by Shamsoddin & Porté-Agel [20]. Recently, Liu & Stevens [11] found that the power output of a wind turbine can also be increased significantly by an upstream hill, provided that the hub height is more than twice as high as the hill.

Hills also affect the downstream development of the wind turbine wake due to the hill-induced pressure gradient and increased turbulence intensity in the hill wake [3]. In general, the wind-turbine wakes tend to follow the terrain topography [5,6,20]. The wake created by a wind turbine sited upstream of a hill recovers faster than in flat terrain due to the favorable pressure gradient created by the hill [10]. Approaching the hilltop, the wake recovery rate decreases due to the adverse pressure gradient on the leeward side of the hill [5,10,11]. The wake recovers faster downstream of the hill due to the increased turbulent intensity [7,8,11]. Hyvärinen & Segalini [9] found that the wind turbine wakes can recover more rapidly in hilly terrain and concluded that undulating hills can have a favorable effect on the wind turbine power production.

The studies mentioned above were performed for neutral conditions. However, during the 24 h diurnal cycle, the atmospheric

* Corresponding author.
** Corresponding author.
E-mail addresses: luoqin.liu@utwente.nl (L. Liu), r.j.a.m.stevens@utwente.nl (R.J.A.M. Stevens).

https://doi.org/10.1016/j.renene.2021.05.035

boundary layer shifts between convective and stable conditions [21]. Even during the short transitions between daytime and nocturnal states, when the atmospheric boundary layer itself is close to neutral, the free atmosphere is often thermally stratified [22–24]. Several studies have shown that the flow development over complex terrain is strongly affected by the thermal stratification [25–27], and it is well known that thermal stratification influences the development of a wind turbine wake [28–30]. However, the effect of thermal stratification on wind turbine performance in hilly terrain is less well explored. Howard et al. [13] performed wind tunnel measurements on the effect of a three-dimensional hill on the performance of a model wind turbine for different thermal stratifications. They showed that the upstream hill has a negative effect on the power production of a turbine located downstream of the hill. However, depending on thermal stratification conditions, the power fluctuations can be increased or decreased. Englberger & Dörnbrack [16] used LES to study the wake development from a wind turbine located on a hilltop for different thermal stratification. They found that the hill mainly influences the near-wake region, while the stratification also influences the far-wake region.

Field experiments allow one to measure wind turbine performance in realistic conditions, but it can be challenging to isolate various physical effects. This makes it more challenging to fully understand the physical phenomena. In wind tunnel measurements, it is possible to isolate the effect of control parameters. However, it can be challenging to extrapolate results from wind tunnel experiments to utility-scale turbines or realistic atmospheric conditions. High-fidelity simulations offer the possibility to set the control parameters exactly and independently. This allows one to systematically study different physical effects. Therefore, LES has become a valuable research tool to complement field experiments and wind tunnel studies. However, it is worth pointing out that, even though it has been shown that the Coriolis forces can affect wind turbine wakes [31], the Coriolis effect had not been considered by Howard et al. [13] and Englberger & Dörnbrack [16]. The novel aspect of the study is that we use an actuator line model to study the turbine performance behind a three-dimensional hill for stable, neutral, and unstable atmospheric thermal stability conditions. In this work, it will be shown that considering the Coriolis-induced wind veer effect is very important. Furthermore, this simulation strategy allows one to get insight into the effect of the hill wake on the wind turbine power fluctuations and corresponding fluctuations on the forces on the wind turbine blades.

The remainder of the paper is organized as follows. The simulation approach is introduced in section 2. The results are presented in section 3. The conclusions are given in section 4.

2. Simulation approach

2.1. Large eddy simulation method

State of the art LES is used to integrate the spatially-filtered Navier-Stokes equations and the filtered transport equation for the potential temperature [32–36]:

$$\nabla \cdot \tilde{\mathbf{u}} = 0, \tag{1}$$

$$\partial_t \tilde{\mathbf{u}} + \tilde{\omega} \times \tilde{\mathbf{u}} = \mathbf{f}_{\mathrm{wt}} + \mathbf{f}_{\mathrm{ib}} + f_c \mathbf{e}_z \times (\mathbf{G} - \tilde{\mathbf{u}}) + \beta(\tilde{\theta} - \theta_0)\mathbf{e}_z - \nabla \tilde{p} - \nabla \cdot \boldsymbol{\tau}, \tag{2}$$

$$\partial_t \tilde{\theta} + \tilde{\mathbf{u}} \cdot \nabla \tilde{\theta} = Q_{\mathrm{ib}} - \nabla \cdot \mathbf{q}. \tag{3}$$

Here, the tilde denotes spatial filtering at a scale of Δ, $\tilde{\mathbf{u}}$ is the velocity, $\tilde{\omega} = \nabla \times \tilde{\mathbf{u}}$ is the vorticity, $\mathbf{f}_{\mathrm{wt}}$ and $\mathbf{f}_{\mathrm{ib}}$ are the forces due to the wind turbine and the immersed boundary, respectively, Q_{ib} is the equivalent heat source due to the immersed boundary, $\tilde{p}$ is the modified pressure, f_c is the Coriolis parameter, $\tilde{\theta}$ is the potential temperature, $\beta = g/\theta_0$ is the buoyancy parameter with g as the gravity acceleration and θ_0 the reference potential temperature, $\mathbf{G} = (U_g, V_g, 0)$ is the geostrophic wind velocity, $\boldsymbol{\tau}$ denotes the deviatoric part of the sub-grid scale shear stress, and q represents the sub-grid scale heat flux. Molecular viscous terms in the governing equations are neglected as the Reynolds number is assumed to be very high. Time integration is performed by a second-order Adams–Bashforth method. The concurrent precursor method is used in both the streamwise and spanwise directions to generate the inflow conditions [35,37]. The Lagrangian-averaging scale-dependent model [33] extended to the scalar case [34,38], which is suitable to simulate the flow-through wind turbines [39] or over complex terrains [40], is used. The code has been validated by Gadde et al. [41] for stable, neutral, and convective atmospheric boundary layers.

A pseudo-spectral discretization is employed in the horizontal periodic directions, and a staggered second-order finite difference method is used in the vertical direction. The first vertical velocity grid plane is located at the ground, while the first horizontal velocity plane is located at half a grid distance above the ground. At the top boundary, the vertical velocity, the sub-grid scale shear stress, and the sub-grid scale heat flux are enforced to zero, while a constant vertical temperature gradient is imposed. In the top 25% of the domain a Rayleigh damping layer is used to reduce gravity waves [38,42]. At the bottom boundary, a wall model based on the Monin-Obukhov similarity theory for both the velocity field and the potential temperature field [34,38,43] is employed,

$$u_* = \frac{\kappa \sqrt{\langle \tilde{u} \rangle^2 + \langle \tilde{v} \rangle^2}}{\ln(z/z_0) - \psi_m}, \quad q_* = \frac{\kappa u_* (\theta_s - \langle \tilde{\theta} \rangle)}{\ln(z/z_0) - \psi_h}, \tag{4}$$

where $\langle \cdot \rangle$ denotes filtering at a scale of 2Δ, $-u_*^2$ is the wall sub-grid scale shear stress, $\kappa = 0.4$ is the von Kármán constant, z is the vertical distance from the wall, z_0 is the roughness height, q_* is the wall sub-grid scale heat flux, θ_s is the potential temperature at the wall surface, and ψ_m and ψ_h are, respectively, the stability corrections for the momentum and heat fluxes [21,44],

$$\psi_m = \begin{cases} -4.8 z/L, & z/L \geq 0, \\ \ln \dfrac{(1+\zeta^2)(1+\zeta)^2}{8} - 2\arctan\zeta + \dfrac{\pi}{2}, & z/L < 0, \end{cases} \tag{5}$$

and

$$\psi_h = \begin{cases} -7.8 z/L, & z/L \geq 0, \\ 2 \ln \dfrac{1+\zeta^2}{2}, & z/L < 0. \end{cases} \tag{6}$$

Here $L = -(u_*^3 \theta_s)/(\kappa g q_*)$ is the Obukhov length and $\zeta = (1 - 15 z/L)^{1/4}$. The hill effect is modeled using a recently developed immersed boundary method that has been validated against experimental data [36]. A constant cooling rate is enforced both on the surface and inside the hill. On the hill surface, the boundary conditions, see Eq. (4), are enforced based on the local values instead of the filtered quantities [36,45].

2.2. Wind turbine model

The actuator line model is used to simulate the wind turbine [46]. The velocities (u_x, u_y, y_z) are interpolated to the actuator points in the global coordinate system (x, y, z) using trilinear interpolation. Subsequently, the local relative azimuthal velocity u_θ is defined in the local coordinate system (r, θ, x) of the blade as follows

$$u_\theta = \Omega r - u_y \cos\theta + u_z \sin\theta, \tag{7}$$

where Ω is the rotor rotation speed, r is the radial location, and θ is the azimuthal angle. The angle of attack α for each actuator line point is

$$\alpha = \varphi - \gamma, \quad \varphi = \arctan\left(\frac{u_x}{u_\theta}\right), \tag{8}$$

where γ is the twist angle of the blade and φ is the relative angle deviation. The lift and drag forces per unit span are

$$f_L = \frac{1}{2}\rho u_{\mathrm{rel}}^2 c C_l, \quad f_D = \frac{1}{2}\rho u_{\mathrm{rel}}^2 c C_d, \tag{9}$$

where ρ is the density of fluid, $u_{\mathrm{rel}} = \sqrt{u_\theta^2 + u_x^2}$ is the velocity relative to the rotating blade, c is the chord length, and C_l and C_d are the lift and drag coefficients that can be obtained from tabulated aerofoil data. For the NREL 5 MW wind turbine to be considered below, C_l and C_d have been corrected for three-dimensional effects [47]. Then the forces in the global coordinate system are

$$\begin{aligned} f_x &= -(f_L \cos\varphi + f_D \sin\varphi), \\ f_y &= -(f_L \sin\varphi - f_D \cos\varphi)\cos\theta, \\ f_z &= (f_L \sin\varphi - f_D \cos\varphi)\sin\theta. \end{aligned} \tag{10}$$

These forces are subsequently transferred to the global coordinate system by using the standard force projection method that is used for actuator line model [46],

$$\eta_\varepsilon = \frac{1}{\pi^{3/2}\varepsilon^3} e^{-r^2/\varepsilon^2}, \tag{11}$$

where r is the distance between the grid location and the actuator line point from which the force originates, and $\varepsilon = 2.5\Delta x$ with Δx the grid size in streamwise direction [48]. The turbine rotation speed is fixed at $\Omega = 9.1552$ RPM. The effects of nacelle and tower are not considered in this study.

2.3. Adjustment of geostrophic wind direction

A controller is used to align the incoming wind direction with the hill and wind turbine. The following P controller is used

$$\Omega_{\mathrm{eff}} = K_p e(t), \quad \alpha(t) = K_p \int_0^t e(\tau)\mathrm{d}\tau, \tag{12}$$

where Ω_{eff} is the effective rotation speed of the reference frame, α is the angle of the overlying geostrophic wind direction, $e(t)$ is the difference between the wind angle at hub height and its reference value, and $K_p = 1 \times 10^{-4}\ \mathrm{s}^{-1}$ is the proportional gain parameter. The momentum equation (2) is modified accordingly as [49],

$$\begin{aligned} \partial_t \tilde{\mathbf{u}} + \tilde{\boldsymbol{\omega}} \times \tilde{\mathbf{u}} = \mathbf{f}_{\mathrm{wt}} + \mathbf{f}_{\mathrm{ib}} + f_c \mathbf{e}_z \times (\mathbf{G} - \tilde{\mathbf{u}}) - \Omega_{\mathrm{eff}} \mathbf{e}_z \times \tilde{\mathbf{u}} \\ + \beta(\tilde{\theta} - \theta_0)\mathbf{e}_z - \nabla\tilde{p} - \nabla\cdot\boldsymbol{\tau}, \end{aligned} \tag{13}$$

and the geostrophic velocity is updated as

$$U_g = G\cos\alpha, \quad V_g = -G\sin\alpha. \tag{14}$$

2.4. Considered cases

Similar to Howard et al. [13], a stable, neutral, and convective boundary layer case are considered in this study. For each thermal stability case, the flow around a three-dimensional hill, the flow around a stand-alone wind turbine, and the case in which the turbine is located behind the hill are simulated, see Fig. 1. One of the limitation of the wind-tunnel experiment by Howard et al. [13] is that it's difficult to extrapolate their findings from the model wind turbine size with a diameter of 0.128 m to the scale of utility-scale wind turbines. Therefore, this study considers the NREL 5 MW reference wind turbine, which has a turbine diameter $D = 126$ m [47]. The hill shape is given by

$$\frac{z_w(x,y)}{h} = \cos^2\left(\frac{\pi\sqrt{x^2+y^2}}{2l}\right), \quad \sqrt{x^2+y^2} \le l, \tag{15}$$

where z_w is the vertical coordinate of the hill surface, and $h = 90$ m and $l = 2.5h$ are the height and half-width of the hill, respectively. Note that the hill height is the same as the wind turbine hub height. The computational domain size is $32h \times 16h \times 8h$ and the grid resolution is $512 \times 256 \times 256$, such that both the hill wake [36] and turbine wake [50] are well resolved.

For the stable case, the standard GEWEX Atmospheric Boundary Layer Study (GABLS) case is selected as it is a well-established benchmark case that is well tested in LES [31,38,51]. This case represents a typical quasi-equilibrium moderately stable ABL, similar to those commonly observed over polar regions and equilibrium nighttime conditions over land in mid-latitudes. The simulations are initialized with a constant streamwise velocity equal to the geostrophic wind speed $G = 8$ m/s. The initial potential temperature profile consists of a mixed layer (with potential temperature 265 K) up to 100 m with an overlying inversion layer with a strength of $\Gamma = 10$ K/km. The surface roughness length for momentum and heat is set to $z_0 = 0.1$ m, the reference potential temperature is $\theta_0 = 263.5$ K, and the Coriolis parameter is $f_c = 1.39 \times 10^{-4}$ rad/s. The surface (ground level) potential temperature is reduced at a prescribed surface cooling rate of $C_r = 0.25$ K/h.

It was shown by Gadde & Stevens [41] that a constant cooling rate $C_r = 0$ K/h results in a boundary layer that is very similar to a (conventionally) neutral boundary layer. This was further confirmed by measuring the surface heat flux q_*, which is negligibly small. Furthermore, it was shown by Kumar et al. [52] that LES cases driven by a constant surface temperature or a constant heat flux produce very similar results. Therefore, to keep the simulation strategy consistent among the stable, neutral, and convective boundary layer cases, the authors decided to vary the atmospheric thermal stability by changing the cooling rate at the ground. A neutral boundary layer is obtained by setting the cooling rate $C_r = 0$ K/h, and $C_r = -0.25$ K/h is used for the convective case. All simulations are run for 9 h, and the statistics are computed during the final hour.

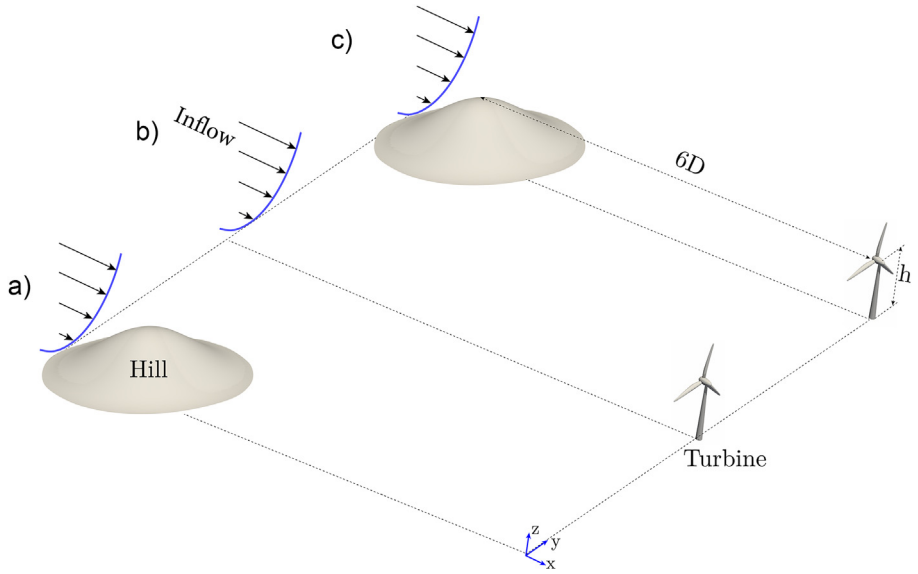

Fig. 1. The three configurations, i.e. the references cases (a) a stand-alone hill and (b) a stand-alone turbine, and (c) the case in which the turbine is placed behind the hill, considered in this study. For each configuration a stable, neutral, and convective boundary layer case is considered; see details in the text. The hill height h, the rotor diameter D, and the distance between the hill and turbine are indicated in the sketch.

3. Simulation results

3.1. Reference atmospheric flow in flat terrain

Fig. 2 (a) shows that there is a low-level jet with a maximum wind speed at $z/h \approx 1.8$ for the stable boundary layer (SBL). This height is similar to the maximum height the blade tip can reach, which is $1.7h$ for the NREL 5 MW turbine. For the neutral boundary layer (NBL) case, the low level jet height is $z/h \approx 2.6$, while there is no low level jet for the convective boundary layer (CBL). The wind

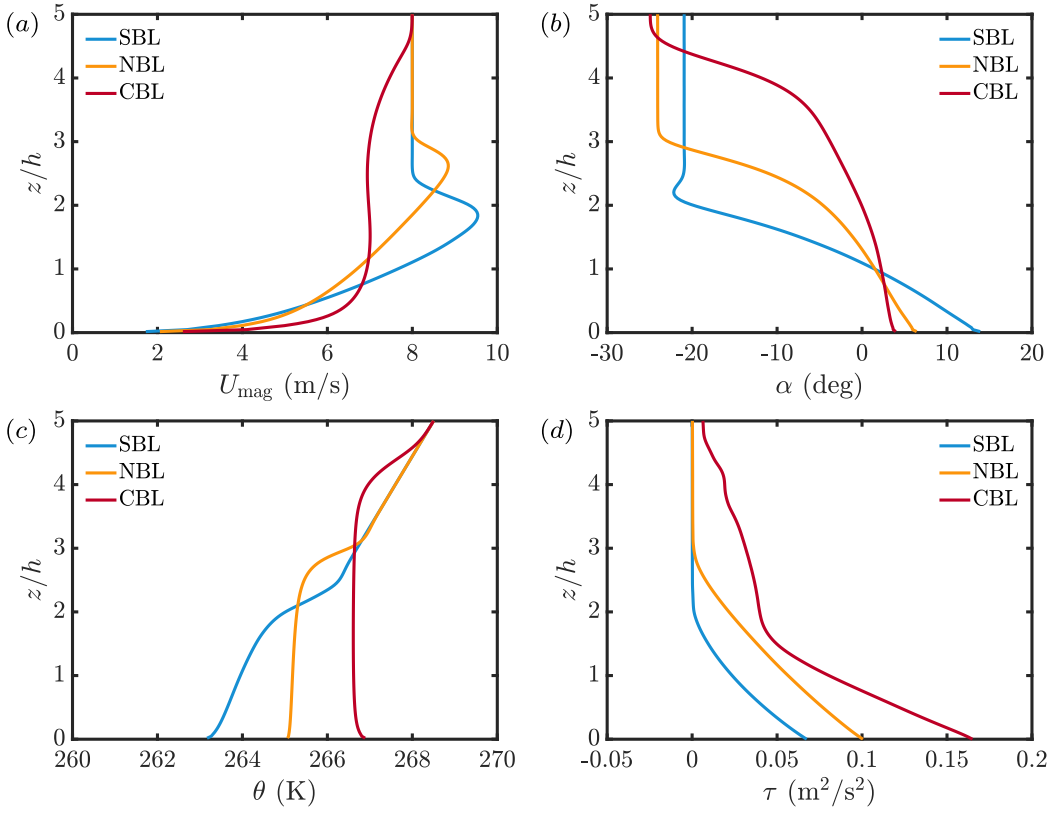

Fig. 2. Vertical profiles of the (a) mean wind speed $U_{\mathrm{mag}} = \sqrt{U^2 + V^2 + W^2}$, where U, V, W are the mean streamwise, spanwise, and vertical velocities, respectively, (b) the wind angle $\alpha = \arctan(V/U)$, (c) the potential temperature θ, and (d) the total momentum flux τ for the stable, neutral, and convective cases.

Table 1
Integral boundary layer properties for the stable, neutral, and convective boundary layer considered in this study. C_r is the cooling rate on the surface, u_* is the friction velocity, q_* is the surface heat flux, δ is the boundary layer thickness defined by the height at which the total momentum flux reaches 5% of the surface value, L is the Obukhov length scale, U_h is the wind speed at the hub height, and $\mathrm{TI} = \sigma / U_h$ is the turbulence intensity at hub height. Here $\sigma = \sqrt{u'^2 + v'^2 + w'^2}$ is the velocity variance, and u', v', w' denote the streamwise, spanwise and vertical velocity fluctuations.

Case	C_r (K/h)	u_* (m/s)	q_* (K•m/s)	δ (m)	L (m)	U_h (m/s)	TI (%)
SBL	0.25	0.260	−0.011	163	108	7.66	6.02
NBL	0	0.317	−0.003	237	730	6.70	9.86
CBL	−0.25	0.406	0.014	419	−319	6.93	11.0

veer and potential temperature gradient are strongest in the SBL and weakest in the CBL (Fig. 2b and c). As a result, the total momentum flux τ is smallest in the SBL and largest in the CBL (Fig. 2d). Table 1 presents various integral boundary layer properties for the SBL, NBL, and CBL case under consideration. In agreement with the above observations, the table shows that the turbulence intensity at hub height increases when the cooling rate is decreased.

3.2. Effect of three-dimensional hill

Fig. 3a shows the vertical time-averaged velocity magnitude deficit profile created for different downstream locations along the symmetry axis of the hill ($y/h = 0$). The figure reveals that due to flow induction, the velocity in front of the hill is slightly reduced compared to the reference case without the hill. This induction effect is very similar to the three thermal stability cases considered here. The speedup of the flow at the top of the hill increases when the cooling rate is decreased as the wind shear is weaker for these cases (see Fig. 2a). On the leeward side of the hill ($x/D = 2$) there is a pronounced hill wake, and surprisingly we find that the strength of the hill wake increases when the cooling rate at the surface is decreased. However, the most interesting phenomenon is the speedup of the flow for the SBL case at $x/D \geq 4$.

Fig. 4 shows the velocity deficit and the turbulence intensity induced by the hill in the horizontal plane at $z/h = 0.75$, i.e. at a height close to the top of the hill. In agreement with Fig. 2b, the deflection of the hill wake increases when the thermal stratification is increased. The figure confirms that while the hill wake is symmetric in convective conditions, it is strongly asymmetric for the SBL case. This asymmetry is caused by the strong wind veer formed in a SBL, see Fig. 2. This confirms the assumption mentioned above that it is essential to consider the Coriolis force in thermally stratified flows when simulating the development of wind turbine wakes near hills. Fig. 4 also shows that the turbulence intensity is strongly increased in the hill wake, especially for the CBL case.

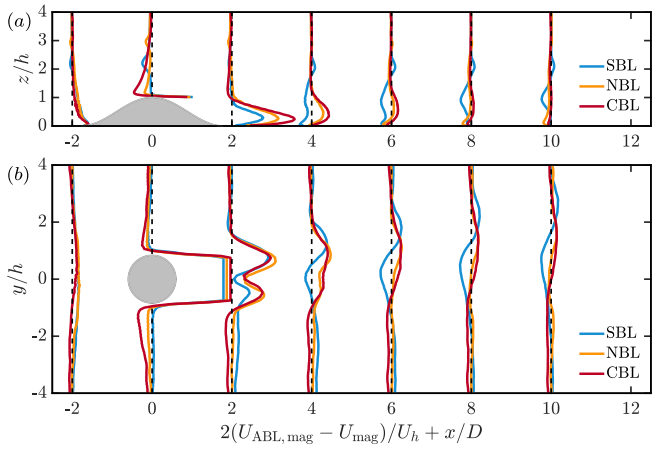

Fig. 3. Profiles of time-averaged velocity magnitude deficit $2(U_{\mathrm{mag,ABL}} - U_{\mathrm{mag}})/U_h + x/D$ for the flow over a three-dimensional hill for (a) $y/h = 0$ and (b) $z/h = 3/4$ and different downstream locations. The subscript "ABL" denotes the corresponding reference case without hill.

Figs. 3 and 4 indicate that there is a very pronounced flow speedup in the SBL case further downstream of the hill. This speedup is caused by the interaction between the wind veer, the low level jet, and the vortex shedding caused by the hill. To illustrate this, a snapshot of the streamwise velocity is shown in Fig. 5a and two-dimensional maps of the time-averaged velocity magnitude at $x/D = 2$ (Fig. 5b) and $x/D = 6$ (Fig. 5c) downstream of the hill for the SBL case. Just behind the hill, the effect of the hill wake is very pronounced. However, six turbine diameters downstream (Fig. 5c) the flow speeds up. The speedup is a result of vortex shedding created by the hill due to which the right side of the hill wake ($y/h > 0$), which has been deflected by the wind veer, entrains high-velocity wind from the low level jet. This happens because the low level jet is located just above the hill due to the strong, stable stratification. Because of the wind veer, the left side of the hill wake ($y/h < 0$) is further replenished by the local upstream flow while the right side is directed further rightwards. As a result, the left side of the hill wake recovers faster than its right side.

Note that the low level jet has to be just above the hill to see such a pronounced flow speedup. As there is no low level jet for the CBL case and the low level jet is too weak and far above the hill for the NBL under consideration, see Fig. 2a, no appreciable flow speedup is observed for these cases. However, for the NBL the wind veer is strong enough to deflect the hill wake such that the wind turbine does not experience the full hill wake effects.

3.3. Wind turbine performance in flat terrain and behind a hill

Fig. 6 shows the time history of the power output of the standalone wind turbine and when the wind turbine is placed behind the hill for the final hour of the simulation when the quasi-equilibrium state has been reached. Table 2 presents the time-averaged power output of the NREL 5 MW wind turbine for the different cases. Consistent with Table 1 and Fig. 2a, which show that the velocity at hub height is strongest for the SBL and weakest for the NBL, the power production of the turbine is highest for the SBL case and lowest for the NBL case. Furthermore, the table shows that the standard deviation of the power production is higher for the CBL case than for the SBL case. This agrees with the trend that the turbulence intensity at hub height is highest for the CBL case.

Interestingly, for the SBL case, the wind turbine power output is significantly higher when it is placed behind the hill than for the reference case without a hill. The reason for this surprising result is the flow speedup due to kinetic energy entrainment from the low level jet, see also Fig. 3. Table 2 reveals that the increase in power production is 24.2% for the case considered here, while also the power fluctuations are increased. For the NBL case, the wind veer is strong enough to deflect the hill wake such that the power output of the downstream turbine is not affected. However, Table 2 reveals that the normalized power fluctuations of the turbine are increased by about 60% compared to the reference case without the hill. For the CBL case, the wind veer is too weak to deflect the hill wake significantly. As a result of the hill wake effect, the power production is much lower, i.e., 34.8%, while the normalized power fluctuations are increased by about 70% compared to the reference case without the hill, see Table 2.

The actuator line model enables one to investigate the aerodynamic loads along the turbine blade, which are plotted in Fig. 7. Fig. 7c,d show that the aerodynamic lift and drag are nearly the

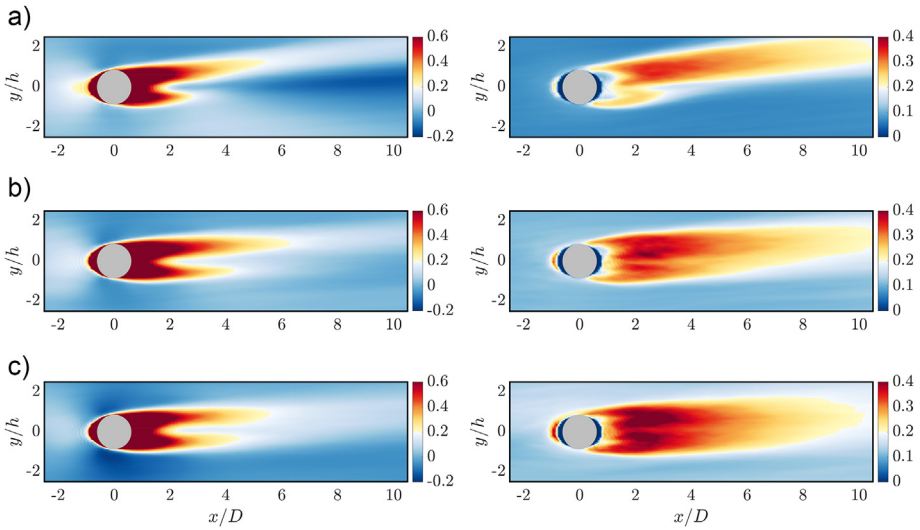

Fig. 4. Left panels show the time-averaged velocity magnitude deficit $(U_{\mathrm{mag,ABL}} - U_{\mathrm{mag}})/U_h$ for flow over a three-dimensional hill compared to the flow without hill at $z/h = 3/4$. The right panels show the corresponding turbulence intensity $\mathrm{TI} = \sigma/U_h$. Top panels: SBL (a), middle panels: NBL (b), lower panels: CBL (c).

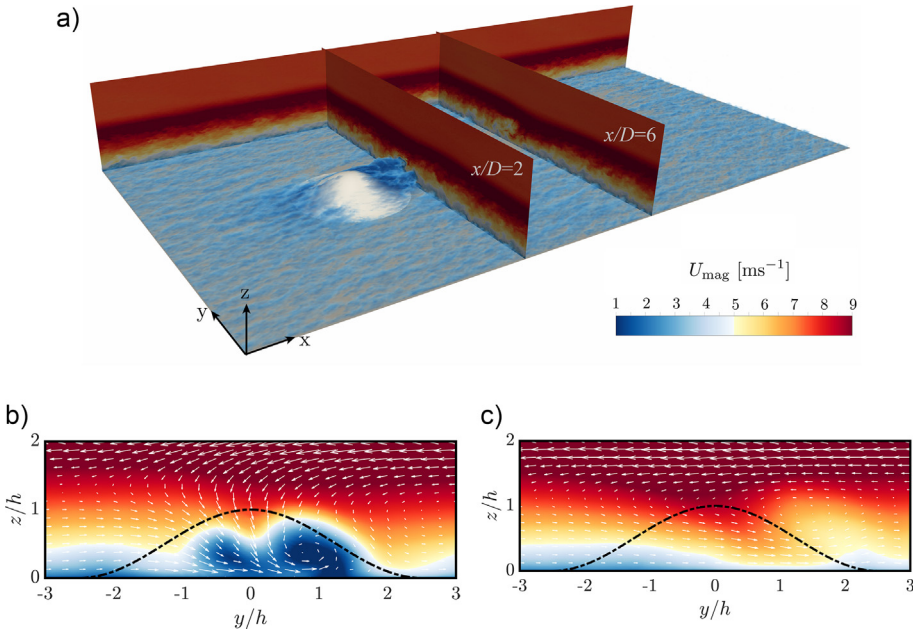

Fig. 5. (a) The instantaneous streamwise velocity for flow over a hill in the SBL case. (b, c) The time-averaged velocity magnitude U_{mag} in the indicated downstream planes at (b) $x/D = 2$ and (c) $x/D = 6$ downwind of the hill. The black dashed line represents the shape of the hill and the white arrows indicate the velocity vector field (V, W) in the plane.

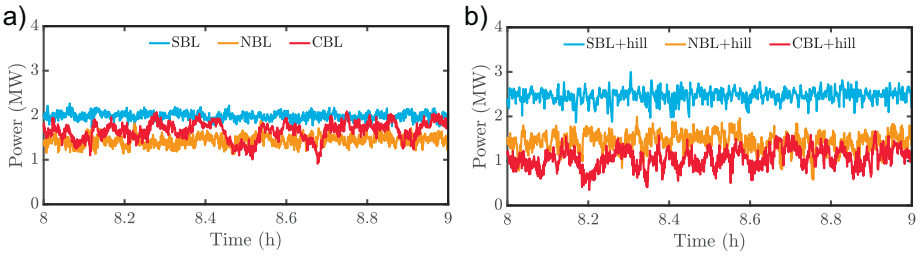

Fig. 6. Time history of the power production of the NREL 5 MW wind turbine in the SBL, NBL, and CBL case. Panel (a) shows the results for the stand-alone wind turbine and (b) when the wind turbine is located behind the hill.

Table 2
Time-averaged power production of the NREL 5 MW wind turbine for the stable, neutral, and convective boundary layer cases considered here. P_1: power output of the stand-alone wind turbine; P_2 the power output when the turbine is located behind the hill. The corresponding normalized standard deviation (indicated by 'std') for the different cases is also reported.

Case	P_1 (MW)	P_1^{std}/P_1 (%)	Case	P_2 (MW)	P_2^{std}/P_2 (%)	$(P_2-P_1)/P_1$ (%)
SBL	1.98	4.0	SBL + hill	2.46	5.7	24.2
NBL	1.43	8.3	NBL + hill	1.44	13.3	0.7
CBL	1.64	12.5	CBL + hill	1.06	21.0	−34.8

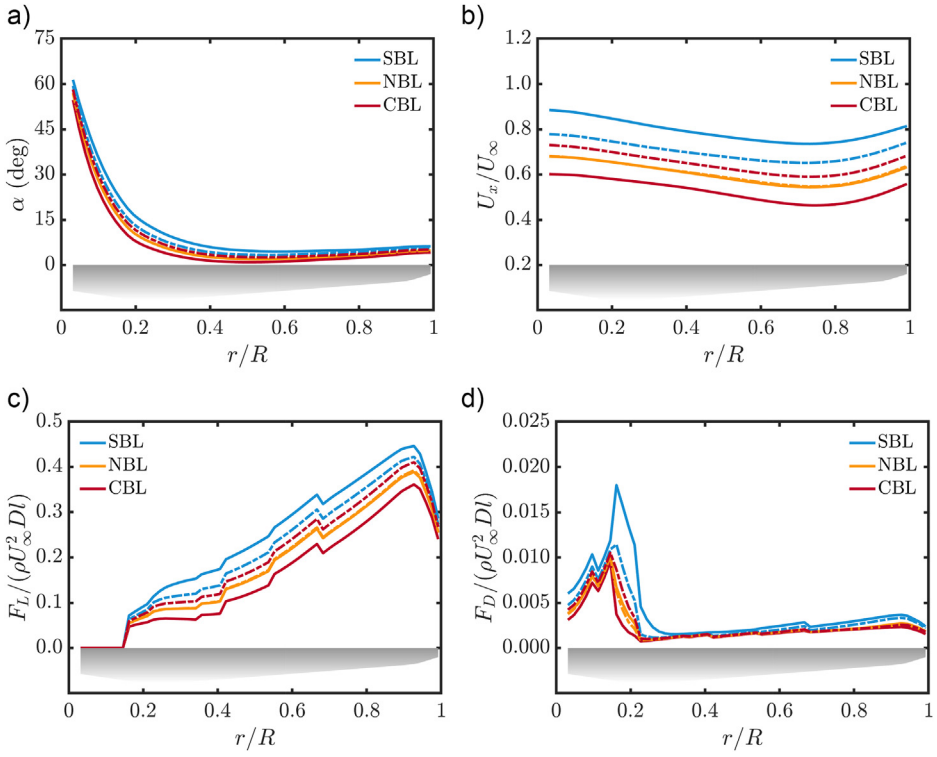

Fig. 7. (a) The angle of attack, (b) the normalized axial velocity, (c) the non-dimensional lift, and (d) the drag per unit span along the blade. Dashed lines: the stand-alone wind turbine case; solid lines: the case in which the turbine is located behind the hill.

same for the stand-alone turbine and the turbine behind the hill for neutral stratification. This conclusion is also valid for other blade variables, e.g., the angle of attack and the axial velocity (Fig. 7a and b). For the stable case, the axial velocity is increased significantly by the upstream hill (Fig. 7b) since the wind veer turns the hill wake away and the low level jet just above the hill is entrained into the hill-shade region. As the angle of attack is also increased slightly by the upstream hill (Fig. 7a) the aerodynamic loads (Fig. 7c,d) and the resultant power production (Fig. 6) are increased accordingly. In contrast, for the convective case, the axial velocity is decreased significantly by the upstream hill (Fig. 7b) since the wind veer is too weak to turn the hill wake away. As a result, both the angle of attack (Fig. 7a), the aerodynamic loads (Fig. 7c,d), and the power production (Fig. 6) are reduced correspondingly.

The results in Fig. 7 confirm that the mean blade quantities are not affected by the upstream hill for the neutral case as the hill wake is deflected. However, it is essential to note that Fig. 8 shows that the increased turbulence intensity created by the upstream hill leads to increased fluctuations in the normalized axial velocity and wind angle at the blades. Due to these stronger velocity fluctuations, the normalized lift and drag force fluctuations also increase. Moreover, this increase in the lift and drag force fluctuations explains the increased power fluctuations, see Fig. 6 and Table 2. The increased fluctuations in the normalized forces experienced by the blades suggest that the turbines are experiencing higher fatigue loading, which could pose hazardous structural threats to wind turbine blades. For this case, the thrust fluctuations increase by about 75%, while the normalized power fluctuations increase only 60%. This indicates that normalized power fluctuations may not fully reflect the increase in the force fluctuations to which the wind turbine blades are exposed.

Thermal stratification can also affect the development of the wind turbine wake. To illustrate it, Fig. 9 shows the normalized velocity deficit in the lateral cross-sectional planes at $(x-x_t)/D = 1, 3, 5$ downwind of the turbine. In the SBL the wake is strongly skewed due to the wind veer. The wake is strongest near the top of the rotor swept area as the wind speed near the rotor top is significantly higher than closer to the ground, see Fig. 2a. As the nacelle has not been included in the simulations, the wake deficit in the wake center is smallest in the near wake ($(x-x_t)/D = 1$), see Fig. 9a. However, further downstream the wake deficit is strongest in the wake center, see Fig. 9a at $(x-x_t)/D = 5$. The wake development under neutral conditions is similar to what is discussed above for the SBL. However, an important difference is that the tilt of the wind turbine wake is less pronounced as wind veer for the neutral case is less than for the SBL, see Fig. 2b. For convective conditions, the wake is almost symmetric with respect to the wake center at $(x-x_t)/D = 1$ (Fig. 9c) as there is almost no wind veer, see Fig. 2b.

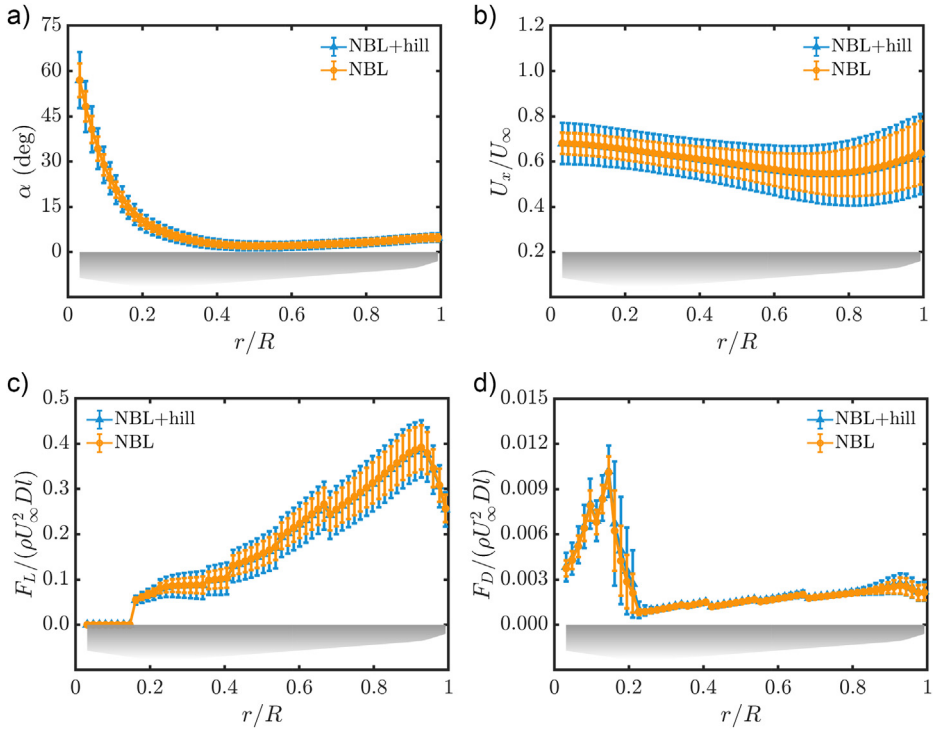

Fig. 8. Mean and standard deviation (indicated by the vertical bars) of (a) the angle of attack, (b) the normalized axial velocity, (c) the non-dimensional lift, and (d) the drag per unit span along the blade.

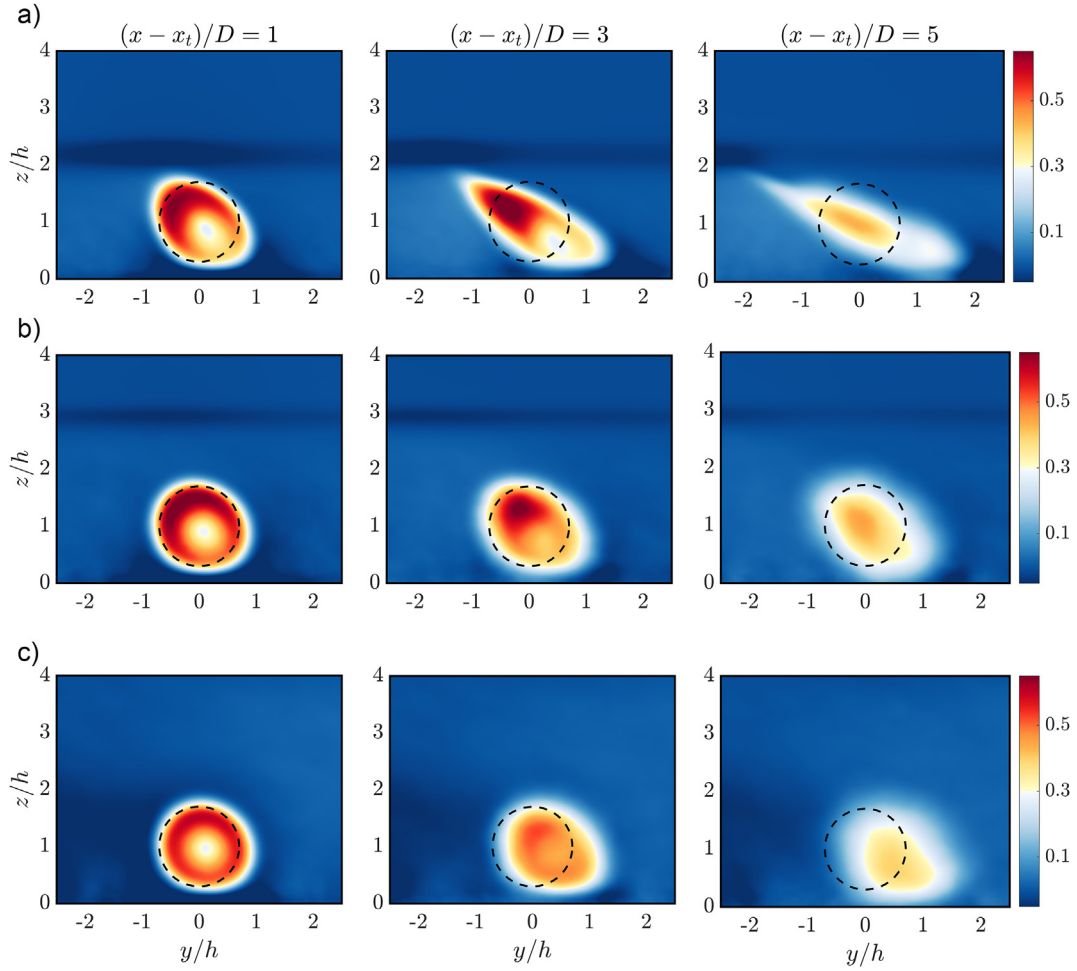

Fig. 9. Contour plots of normalized velocity deficit $(U_{\mathrm{ABL,mag}} - U_{\mathrm{mag}})/U_h$ in the vertical (y,z) planes at $(x-x_t)/D = 1, 3, 5$ downwind of the NREL 5 MW wind turbine under (a) stable, (b) neutral, and (c) convective atmospheric stability. Here $U_{\mathrm{ABL,mag}}$ indicates the reference flow without wind turbine, x_t is the streamwise location of the turbine, and the dashed circle indicates the location of the upstream turbine.

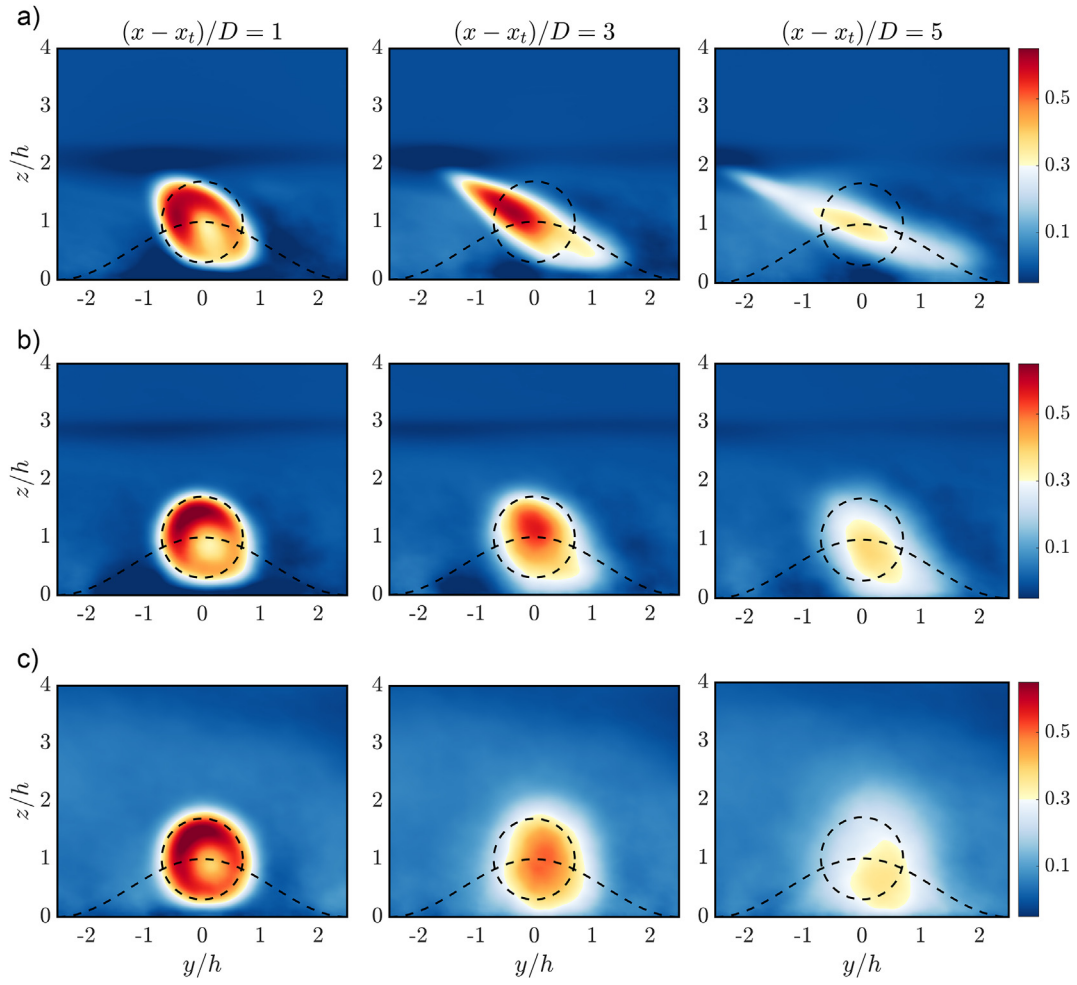

Fig. 10. Contour plots of normalized velocity deficit $(U_{\text{hill,mag}} - U_{\text{mag}})/U_h$ in the vertical (y,z) planes at $(x - x_t)/D = 1, 3, 5$ downwind of the NREL 5 MW wind turbine under (a) stable, (b) neutral, and (c) convective atmospheric stability. Here $U_{\text{hill,mag}}$ denotes the mean velocity magnitude of the reference flow over the hill without the turbine, x_t is the streamwise location of the turbine, and the dashed lines indicate the location of the upstream hill and turbine.

Fig. 10 shows the corresponding wake maps for the cases in which the turbine is placed behind the hill. A comparison with Fig. 9 reveals that effect of the hill wake on the near wake of the turbine is limited. However, further downstream $(x - x_t)/D \geq 3$ the influence of the hill on the wake development becomes more noticeable as the wakes recover faster than for the case without hill due to the increased mixing that is induced by the hill wake. This effect is most pronounced for the CBL case.

4. Conclusions

The effect of a three-dimensional hill on the performance of a wind turbine located six turbine diameters downstream of the hill is studied using state-of-the-art large eddy simulations. Three different thermal stratifications are considered, namely, stable, neutral, and convective atmospheric conditions. The results show that it is crucial to account for the Coriolis-induced wind veer when simulating the development of wind turbine wakes in the vicinity of a hill. The wind veer can significantly deflect the hill wake. Furthermore, the vortex shedding induced by the hill can result in the entrainment of the high-velocity wind from the low level jet to the turbine area. This can result in an unexpected increase in the turbine power production compared to the reference case without hill.

It is shown that the hill wake significantly increases the wind turbine power fluctuations, even when the turbine is not directly located in the hill wake, which is the case for the neutral boundary layer case considered here. The increased turbulence intensity by the hill results in increased velocity fluctuations along the blades. These stronger velocity fluctuations at the blades lead to higher fluctuations in the lift and drag forces experienced by the blades. For the neutral boundary layer case, the power fluctuations increase by 60%, while the increase in the thrust fluctuations is 75% due to the hill induced turbulence. This increase in the normalized lift and drag force fluctuations to which the blades are exposed suggests that the turbines experience higher fatigue loading. It is shown that the increase in the power fluctuations may not fully reflect the increase in the local forces experienced by the blades, and more research to investigate this effect further is required.

CRediT authorship contribution statement

Luoqin Liu: Conceptualization, Data curation, Formal analysis, Investigation, Methodology, Software, Validation, Visualization, Writing – original draft, Writing – review & editing. **Richard J.A.M. Stevens:** Conceptualization, Funding acquisition, Methodology, Software, Supervision, Visualization, Writing – review & editing.

Declaration of competing interest

The authors declare that they have no known competing financial interests or personal relationships that could have appeared to influence the work reported in this paper.

Acknowledgements

The authors thank Srinidhi N. Gadde for drawing Fig. 1 and Fig. 5a, as well as insightful discussions. This work is part of the Shell-NWO/FOM-initiative Computational sciences for energy research of Shell and Chemical Sciences, Earth, and Live Sciences, Physical Sciences, FOM, and STW, and an STW VIDI Grant (No. 14868). This work was carried out on the national e-infrastructure of SURFsara, a subsidiary of SURF corporation, the collaborative ICT organization for Dutch education and research. The authors acknowledge PRACE for awarding them access to Galileo at CINECA, Italy.

References

[1] P.H. Alfredsson, A. Segalini, Wind farms in complex terrains: an introduction, Phil. Trans. R. Soc. A 375 (2017) 20160096.
[2] R.J.A.M. Stevens, C. Meneveau, Flow structure and turbulence in wind farms, Annu. Rev. Fluid Mech. 49 (2017) 311–339.
[3] F. Porté-Agel, M. Bastankhah, S. Shamsoddin, Wind-turbine and wind-farm flows: a review, Boundary-Layer Meteorol. 74 (2020) 1–59.
[4] G.J. Taylor, D. Smith, Wake measurements over complex terrain, in: Proceedings of the 13th British Wind Energy Association Conference, 10-12 April, Swansea, UK, 1991, pp. 335–342.
[5] E.S. Politis, J. Prospathopoulos, D. Cabezon, K.S. Hansen, P. Chaviaropoulos, R.J. Barthelmie, Modeling wake effects in large wind farms in complex terrain: the problem, the methods and the issues, Wind Energy 15 (2012) 161–182.
[6] W. Tian, A. Ozbay, W. Yuan, P. Sarakar, H. Hu, An experimental study on the performances of wind turbines over complex terrains, in: 51st AIAA Aerospace Sciences Meeting Including the New Horizons Forum and Aerospace Exposition, 07-10 January, Grapevine, Texas, 2013. AIAA 2013–0612.
[7] X. Yang, K.B. Howard, M. Guala, F. Sotiropoulos, Effects of a three-dimensional hill on the wake characteristics of a model wind turbine, Phys. Fluids 27 (2015), 025103.
[8] K.B. Howard, J.S. Hu, L.P. Chamorro, M. Guala, Characterizing the response of a wind turbine model under complex inflow conditions, Wind Energy 18 (2015) 729–743.
[9] A. Hyvärinen, A. Segalini, Effects from complex terrain on wind-turbine performance, J. Energy Resour. Technol. 139 (2017), 051205.
[10] S. Shamsoddin, F. Porté-Agel, Wind turbine wakes over hills, J. Fluid Mech. 855 (2018) 671–702.
[11] L. Liu, R.J.A.M. Stevens, Effects of two-dimensional steep hills on the performance of wind turbines and wind farms, Boundary-Layer Meteorol. 174 (2020a) 61–80.
[12] Z. Liu, S. Lu, T. Ishihara, Large Eddy Simulations of Wind Turbine Wakes in Typical Complex Topographies, Wind Energy, 2020, pp. 1–30.
[13] K.B. Howard, L.P. Chamorro, M. Guala, A comparative analysis on the response of a wind-turbine model to atmospheric and terrain effects, Boundary-Layer Meteorol. 158 (2016) 229–255.
[14] K.S. Hansen, G.C. Larsen, R. Menke, N. Vasiljevic, N. Angelou, J. Feng, W.J. Zhu, A. Vignaroli, W.W. Liu, C. Xu, W.Z. Shen, Wind turbine wake measurement in complex terrain, J. Phys. Conf. Ser. 753 (2016), 032013.
[15] R. Menke, N. Vasiljević, K.S. Hansen, A.N. Hahmann, J. Mann, Does the wind turbine wake follow the topography? A multi-lidar study in complex terrain, Wind Energy Science 3 (2018) 681–691.
[16] A. Englberger, A. Dörnbrack, Wind-turbine wakes responding to stably stratified flow over complex terrain, J. Phys. Conf. Ser. 1037 (2018), 072014.
[17] R.J. Barthelmie, S.C. Pryor, Automated wind turbine wake characterization in complex terrain, Atmos. Meas. Tech. 12 (2019) 3463–3484.
[18] P. Santos, J. Mann, N. Vasiljević, E. Cantero, J.S. Rodrigo, F. Borbón, D. Martínez-Villagrasa, B. Martí, J. Cuxart, The Alaiz experiment: untangling multi-scale stratified flows over complex terrain, Wind Energy Science 5 (2020) 1793–1810.
[19] C.G. Helmis, K.H. Papadopoulos, D.N. Asimakopoulos, P.G. Papageorgas, A.T. Soilemes, An experimental study of the near-wake structure of a wind turbine operating over complex terrain, Sol. Energy 54 (1995) 413–428.
[20] S. Shamsoddin, F. Porté-Agel, Large-eddy simulation of atmospheric boundary-layer flow through a wind farm sited on topography, Boundary-Layer Meteorol. 163 (2017) 1–17.
[21] R.B. Stull, An Introduction to Boundary Layer Meteorology, Kluwer Academic Publishers, Boston, 1988.
[22] S.S. Zilitinkevich, I.N. Esau, On integral measures of the neutral barotropic planetary boundary layer, Boundary-Layer Meteorol. 104 (2002) 371–379.
[23] L. Liu, S.N. Gadde, R.J.A.M. Stevens, Geostrophic drag law for conventionally neutral atmospheric boundary layers revisited, Q. J. R. Meteorol. Soc. 147 (2021a) 847–857.
[24] L. Liu, S.N. Gadde, R.J.A.M. Stevens, Universal wind profile for conventionally neutral atmospheric boundary layers, Phys. Rev. Lett. 126 (2021b) 104502.
[25] A.N. Ross, S. Arnold, S.B. Vosper, S. Mobbs, N. Dixon, A. Robins, A comparison of wind-tunnel experiments and numerical simulations of neutral and stratified flow over a hill, Boundary-Layer Meteorol. 113 (2004) 427–459.
[26] T. Takahashi, S. Kato, S. Murakami, R. Ooka, M. Fassy Yassin, R. Kono, Wind tunnel tests of effects of atmospheric stability on turbulent flow over a three-dimensional hill, J. Wind Eng. Ind. Aerod. 93 (2005) 155–169.
[27] M. Lehner, M. Rotach, Current challenges in understanding and predicting transport and exchange in the atmosphere over mountainous terrain, Atmosphere 9 (2018) 276.
[28] L.P. Chamorro, F. Porté-Agel, Effects of thermal stability and incoming boundary-layer flow characteristics on wind-turbine wakes: a wind-tunnel study, Boundary-Layer Meteorol. 136 (2010) 515–533.
[29] M.J. Churchfield, S. Lee, J. Michalakes, P.J. Moriarty, A numerical study of the effects of atmospheric and wake turbulence on wind turbine dynamics, J. Turb. 13 (2012) 1–32.
[30] N. Ali, G. Cortina, N. Hamilton, M. Calaf, R.B. Cal, Turbulence characteristics of a thermally stratified wind turbine array boundary layer via proper orthogonal decomposition, J. Fluid Mech. 828 (2017) 175–195.
[31] M. Abkar, A. Sharifi, F. Porté-Agel, Wake flow in a wind farm during a diurnal cycle, J. Turb. 17 (2016) 420–441.
[32] J.D. Albertson, Large Eddy Simulation of Land-Atmosphere Interaction, Ph.D. thesis, University of California, 1996.
[33] E. Bou-Zeid, C. Meneveau, M.B. Parlange, A scale-dependent Lagrangian dynamic model for large eddy simulation of complex turbulent flows, Phys. Fluids 17 (2005), 025105.
[34] R. Stoll, F. Porté-Agel, Large-eddy simulation of the stable atmospheric boundary layer using dynamic models with different averaging schemes, Boundary-Layer Meteorol. 126 (2008) 1–28.
[35] S.N. Gadde, R.J.A.M. Stevens, Effect of Coriolis force on a wind farm wake, J. Phys. Conf. Ser. 1256 (2019), 012026.
[36] L. Liu, R.J.A.M. Stevens, Wall modeled immersed boundary method for high Reynolds number flow over complex terrain, Comput. Fluids 208 (2020b) 104604.
[37] R.J.A.M. Stevens, J. Graham, C. Meneveau, A concurrent precursor inflow method for large eddy simulations and applications to finite length wind farms, Renew. Energy 68 (2014) 46–50.
[38] S.N. Gadde, A. Stieren, R.J.A.M. Stevens, Large-eddy simulations of stratified atmospheric boundary layers: comparison of different subgrid models, Boundary-Layer Meteorol. 178 (2021) 363–382.
[39] M. Calaf, C. Meneveau, J. Meyers, Large eddy simulations of fully developed wind-turbine array boundary layers, Phys. Fluids 22 (2010), 015110.
[40] F. Wan, F. Porté-Agel, Large-eddy simulation of stably-stratified flow over a steep hill, Boundary-Layer Meteorol. 138 (2011) 367–384.
[41] S.N. Gadde, R.J.A.M. Stevens, Interaction between low-level jets and wind farms in a stable atmospheric boundary layer, Phys. Rev. Fluids 6 (2021), 014603.
[42] J.B. Klemp, D.K. Lilly, Numerical simulation of hydrostatic mountain waves, J. Atmos. Sci. 35 (1978) 78–107.
[43] C.-H. Moeng, A large-eddy simulation model for the study of planetary boundary-layer turbulence, J. Atmos. Sci. 41 (1984) 2052–2062.
[44] J.A. Businger, J.C. Wyngaard, Y. Izumi, E.F. Bradley, Flux-profile relationships in the atmospheric surface layer, J. Atmos. Sci. 28 (1971) 181–189.
[45] S. Chester, C. Meneveau, M.B. Parlange, Modeling turbulent flow over fractal trees with renormalized numerical simulation, J. Comput. Phys. 225 (2007) 427–448.
[46] J.N. Sørensen, W.Z. Shen, Numerical modeling of wind turbine wakes, J. Fluid Eng. 124 (2002) 393.
[47] J. Jonkman, S. Butterfield, W. Musial, G. Scott, Definition of a 5-MW Reference Wind Turbine for Offshore System Development, National Renewable Energy Laboratory, Golden, Colorado, 2009.
[48] L.A. Martínez-Tossas, M.J. Churchfield, C. Meneveau, Large eddy simulation of wind turbine wakes: detailed comparisons of two codes focusing on effects of numerics and subgrid modeling, J. Phys. Conf. Ser. 625 (2015), 012024.
[49] A. Sescu, C. Meneveau, A control algorithm for statistically stationary large-eddy simulations of thermally stratified boundary layers, Q. J. R. Meteorol. Soc. 140 (2017–2022) (2014).
[50] R.J.A.M. Stevens, L.A. Martínez-Tossas, C. Meneveau, Comparison of wind farm large eddy simulations using actuator disk and actuator line models with wind tunnel experiments, Renew. Energy 116 (2018) 470–478.
[51] R.J. Beare, M.K. Macvean, A.A.M. Holtslag, J. Cuxart, I. Esau, J.-C. Golaz, M.A. Jimenez, M. Khairoutdinov, B. Kosovic, D. Lewellen, T.S. Lund, J.K. Lundquist, A. Mccabe, A.F. Moene, Y. Noh, S. Raasch, P. Sullivan, An intercomparison of large eddy simulations of the stable boundary layer, Boundary-Layer Meteorol. 118 (2006) 247–272.
[52] V. Kumar, G. Svensson, A.A.M. Holtslag, C. Meneveau, M.B. Parlange, Impact of surface flux formulations and geostrophic forcing on large-eddy simulations of diurnal atmospheric boundary layer flow, J. Appl. Meteorol. Climatol. 49 (2010) 1496–1516.